
Assessing interactions in the brain with exact low-resolution electromagnetic tomography

Roberto D. Pascual-Marqui, Dietrich Lehmann, Martha Koukkou, Kieko Kochi, Peter Anderer, Bernd Saletu, Hideaki Tanaka, Koichi Hirata, E. Roy John, Leslie Prichep, Rolando Biscay-Lirio and Toshihiko Kinoshita

Phil. Trans. R. Soc. A 2011 **369**, doi: 10.1098/rsta.2011.0081, published 5 September 2011

Supplementary data

"Data Supplement"

<http://rsta.royalsocietypublishing.org/content/suppl/2011/08/16/369.1952.3768.DC1.html>

References

This article cites 37 articles, 3 of which can be accessed free

<http://rsta.royalsocietypublishing.org/content/369/1952/3768.full.html#ref-list-1>

Article cited in:

<http://rsta.royalsocietypublishing.org/content/369/1952/3768.full.html#related-urls>

Subject collections

Articles on similar topics can be found in the following collections

[image processing](#) (13 articles)

[medical physics](#) (23 articles)

Email alerting service

Receive free email alerts when new articles cite this article - sign up in the box at the top right-hand corner of the article or click [here](#)

Assessing interactions in the brain with exact low-resolution electromagnetic tomography

BY ROBERTO D. PASCUAL-MARQUI^{1,2,*}, DIETRICH LEHMANN¹,
MARTHA KOUKKOU¹, KIEKO KOCHI¹, PETER ANDERER³, BERND SALETU³,
HIDEAKI TANAKA⁴, KOICHI HIRATA⁴, E. ROY JOHN^{5,6}, LESLIE PRICHEP^{5,6},
ROLANDO BISCAY-LIRIO^{7,8} AND TOSHIHIKO KINOSHITA²

¹*The KEY Institute for Brain-Mind Research, University Hospital of Psychiatry, Lengstrasse 31, 8032 Zurich, Switzerland*

²*Department of Neuropsychiatry, Kansai Medical University Hospital, 10-15, Fumizono-cho, Moriguchi, Osaka, 570-8507 Japan*

³*Department of Psychiatry and Psychotherapy, Medical University of Vienna, Austria*

⁴*Department of Neurology, Dokkyo University School of Medicine, Tochigi, Japan*

⁵*Brain Research Laboratories, Department of Psychiatry, New York University School of Medicine, NY, USA*

⁶*Nathan S. Kline Institute for Psychiatric Research, Orangeburg, NY, USA*

⁷*Institute for Cybernetics, Mathematics, and Physics, Havana, Cuba*

⁸*DEUV-CIMFAV, Science Faculty, University of Valparaiso, Chile*

Scalp electric potentials (electroencephalogram; EEG) are contingent to the impressed current density unleashed by cortical pyramidal neurons undergoing post-synaptic processes. EEG neuroimaging consists of estimating the cortical current density from scalp recordings. We report a solution to this inverse problem that attains exact localization: exact low-resolution brain electromagnetic tomography (eLORETA). This non-invasive method yields high time-resolution intracranial signals that can be used for assessing functional dynamic connectivity in the brain, quantified by coherence and phase synchronization. However, these measures are non-physiologically high because of volume conduction and low spatial resolution. We present a new method to solve this problem by decomposing them into instantaneous and lagged components, with the lagged part having almost pure physiological origin.

Keywords: electroencephalogram; low-resolution electromagnetic tomography; functional connectivity; exact low-resolution electromagnetic tomography

*Author for correspondence (pascualm@key.uzh.ch; pascualr@takii.kmu.ac.jp).

Electronic supplementary material is available at <http://dx.doi.org/10.1098/rsta.2011.0081> or via <http://rsta.royalsocietypublishing.org>.

One contribution of 11 to a Theme Issue ‘The complexity of sleep’.

1. Introduction

We aim to use the electroencephalogram (EEG), consisting of high time resolution measurements of scalp electric potential differences, for studying brain function. These measurements are employed for computing the current density on the cortex. The new data now consist of time series of current density, typically sampled at rates of 100–1000 samples per second, and virtually recorded from all over the cortex, at typically 5 mm spatial resolution. This massive amount of data contains essential information on brain function. This poses the problem of how to process and extract information.

Traditionally, topographic scalp maps have been used for studying brain function. Compelling studies that demonstrate the functional brain state information in scalp maps can be found in Lehmann [1], Saletu *et al.* [2] and John *et al.* [3]. However, their use for localization inference is questionable, since cortical electric neuronal activity does not map radially onto the scalp. We emphasize that this problem also applies to the magnetoencephalogram (MEG). This justifies the need for an inverse solution that correctly localizes cortical activity from scalp potentials.

The aims of this study are: (i) to present an inverse solution to the EEG problem that computes cortical current density (i.e. electric neuronal activity), with optimal localization properties, and (ii) to present methods for properly estimating dynamic functional connectivity in the brain based on the estimated current density signals.

2. Electroencephalograms and intracranial current density

(a) General formulation

The intracranial sources of scalp electric potential differences are thought to be cortical pyramidal neurons, which undergo post-synaptic potentials that create an active, impressed current density. The dipolar nature (current density vector) of these sources is documented in Mitzdorf [4] and Martin [5].

The corresponding relation between the current density vector field and the scalp potentials can be expressed as [6]

$$\Phi_c = \mathbf{K}_c \mathbf{J} + c \mathbf{1}, \quad (2.1)$$

where $\Phi_c \in \mathbb{R}^{N_E \times 1}$ denotes the potentials at N_E scalp electrodes, all measured with respect to the same reference electrode; $\mathbf{J} \in \mathbb{R}^{N_V \times 1}$ is the current density at N_V cortical voxels; c is a scalar determined by the reference electrode (which can be arbitrary); $\mathbf{1} \in \mathbb{R}^{N_E \times 1}$ is a vector of ones; and $\mathbf{K}_c \in \mathbb{R}^{N_E \times N_V}$ is the lead field (determined by the geometry and conductivity profile of the head). The subscript ‘c’ in Φ_c and \mathbf{K}_c emphasizes a fact of nature: potentials are determined up to an arbitrary additive constant (which in this case is related to the choice for the reference electrode). Equation (2.1) expresses a deterministic law of physics. Further on, this will be embedded in a stochastic setting, by considering both measurement and biological noise.

Technical details on the definition and computation of the lead field can be found in Sarvas [7] and Fuchs *et al.* [8]. In previous simple simulation studies, such as those reported in Pascual-Marqui [9], a spherical head model was used, for

which analytical expressions exist for the lead field [10]. In this study, the lead field was computed numerically for a realistic head shape, using the boundary-element method [8].

This forward equation corresponds to an instantaneous discrete sampling of the measurement space (scalp electrodes) and the solution space (cortical voxels). For simplicity, we assume that the orientation of the current density vector is known (the general case with full unknown current density vector can be found in Pascual-Marqui [6]).

The inverse problem of interest is the estimation of the unknown electric neuronal activity \mathbf{J} , given the lead field \mathbf{K}_c and the scalp potential measurements Φ_c . The nuisance parameter c , related to the arbitrary choice of the reference electrode, must be accounted for.

(b) *The final solution to the so-called ‘reference electrode problem’*

We first solve the so-called ‘reference electrode problem’, which corresponds to solving

$$c = \arg \min_c \|\Phi_c - \mathbf{K}_c \mathbf{J} - c \mathbf{1}\|^2, \quad (2.2)$$

where $\|\bullet\|$ denotes the Euclidean norm. This means that c must satisfy, as best as possible, the forward equation (2.1). The squared Euclidean distance can be generalized to a Mahalanobis distance using the covariance matrix of the measurement noise. Solving the problem in equation (2.2) and plugging the solution back into equation (2.1) gives

$$(\mathbf{H}\Phi_c) = (\mathbf{H}\mathbf{K}_c)\mathbf{J}, \quad (2.3)$$

where \mathbf{H} is

$$\mathbf{H} = \mathbf{I} - \frac{\mathbf{1}\mathbf{1}^T}{\mathbf{1}^T\mathbf{1}}, \quad (2.4)$$

where the superscript ‘T’ denotes the vector–matrix transpose; and with $\mathbf{I} \in \mathbb{R}^{N_E \times N_E}$ being the identity matrix. The essential property of \mathbf{H} is

$$\mathbf{H}\mathbf{1} \equiv \mathbf{0}. \quad (2.5)$$

The matrix \mathbf{H} is known in statistics as the centring matrix (e.g. [11]), which subtracts the average value.

This has a profound implication, demonstrating that inverse solutions are reference independent as they must be obtained from the reference-independent forward equation (2.3), which is invariant to any change of reference.

Henceforth, the reference-independent forward equation (2.3) will be written as

$$\Phi = \mathbf{K}\mathbf{J}, \quad (2.6)$$

with

$$\Phi = (\mathbf{H}\Phi_c) \quad (2.7)$$

and

$$\mathbf{K} = (\mathbf{H}\mathbf{K}_c). \quad (2.8)$$

The effect of the operator \mathbf{H} is known in the EEG literature as the average reference [6,12].

An important consequence of these initial derivations is the proof that there is no such thing as an ‘ideal reference’, if the aim is localization. Obviously, an inverse solution will change with different samplings (i.e. with the number and the locations of scalp electrodes); but for a given sampling, the solution to a properly posed inverse problem that explicitly models the reference electrode (as in equations (2.1) and (2.2)) will not depend on the choice of the reference.

(c) *The inverse solution*

We seek to solve the linear system of equations (2.6) for the unknown current density \mathbf{J} . From the outset, we clarify that this is a multi-variate problem, analogous, for example, to X-ray tomography [13], which is not solved as a collection of independent univariate least squares for each voxel separately (repeated single dipole fitting).

Typically, the number of electrodes is much smaller than the number of voxels, $N_E \ll N_V$, and the problem is underdetermined, with infinitely many solutions. In a general setting, Helmholtz [14] demonstrated that many different current density distributions exist in three-dimensional space that are consistent with the electric potential distribution on a surface enclosing the volume.

Similar to the setting in equation (2.2), we look for particular linear solutions of the form

$$\mathbf{J} = \arg \min_{\mathbf{J}} \|\Phi - \mathbf{KJ}\|^2 + \alpha \mathbf{J}^T \mathbf{WJ}, \quad (2.9)$$

which is a regularized, weighted minimum norm problem, where $\alpha \geq 0$ is the Tikhonov regularization parameter [15]; and $\mathbf{W} \in \mathbb{R}^{N_V \times N_V}$ is a symmetric positive definite weight matrix (see Pascual-Marqui [16] for a generalization to non-negative definite matrices). It is important to note that the problem in equation (2.9) has at least two different interpretations. On the one hand, it is a conventional form studied in mathematical functional analysis [15]. On the other hand, it can be derived from a Bayesian formulation of the inverse problem [17]. An excellent general review of other functionals for solving the inverse problem can be found in Valdes-Sosa *et al.* [18].

The general solution to the problem in equation (2.9) is

$$\mathbf{J} = \mathbf{W}^{-1} \mathbf{K}^T (\mathbf{KW}^{-1} \mathbf{K}^T + \alpha \mathbf{H})^+ \Phi, \quad (2.10)$$

where the superscript ‘+’ denotes the Moore–Penrose pseudoinverse [19].

Setting $\mathbf{W} = \mathbf{I}$ (identity matrix) gives the classical non-weighted minimum norm solution [20]

$$\mathbf{J} = \mathbf{K}^T (\mathbf{KK}^T + \alpha \mathbf{H})^+ \Phi. \quad (2.11)$$

It was shown in Pascual-Marqui [9], both empirically and theoretically, that the non-weighted minimum norm has very bad localization properties, misplacing deep sources to the surface. The reason is because this solution is a harmonic function that attains its extreme values only at the boundary of the solution space [21]. This basic physics property of the minimum norm invalidates its use for localization, regardless of the fact that it is the simplest solution (see [22]).

In the method known as low-resolution electromagnetic tomography (LORETA) [23], the matrix \mathbf{W} implements the squared three-dimensional spatial Laplacian operator. In its simplest discrete implementation, the Laplacian compares the current density at one voxel with that of its closest neighbours,

as explained in detail in Pascual-Marqui *et al.* [23] and Pascual-Marqui [9]. Minimization of its squared value forces the current density at each voxel to be as similar as possible to that of its neighbours, thus forcing spatial smoothness. This condition is a macroscopic implementation of what occurs at the cellular level: non-negligible EEG is only possible if neighbouring pyramidal neurons are very highly synchronized (e.g. [24]). It should be noted that a three-dimensional Laplacian does not respect smoothness along the cortical surface with its many foldings (e.g. smoothing would occur across opposite walls of a sulcus). A more accurate implementation would consider the Laplacian along the cortical manifold, as in Grova *et al.* [25], where the Laplacian was restricted to the cortical mesh.

It was empirically shown in simulation studies [9], under ideal noiseless conditions, using 148 electrodes and 818 uniformly distributed voxels that LORETA achieves an average localization error of only one voxel unit, uniformly at all depths, when compared with the non-weighted minimum norm that has maximal error for deep sources.

It has been thought that better localization can be achieved with depth-weighted minimum norm, by giving larger weights to deep voxels. A recent attempt in this direction can be found in Lin *et al.* [26], where some improvement is reported. However, the weights only achieve a modest reduction in localization error compared with the minimum norm, as reported in Pascual-Marqui [16].

(d) Standardized current density tomographies

In this approach, after the current density is estimated, a second post-processing step is applied, consisting of the statistical standardization of the current density values. In this sense, localization inference is not based on the estimated current density directly, but on its standardized value, which is unitless.

Typically, these methods use the minimum norm solution as the current density estimator in the first step, which by itself has a large localization error. The statistically standardized current density is defined as

$$z_i = \frac{[\mathbf{J}]_i}{[\mathbf{S}_\mathbf{J}]_{ii}^{1/2}}, \quad (2.12)$$

where $[\mathbf{J}]_i$ is the estimated current density at the i th voxel (e.g. from equation (2.11)); $\mathbf{S}_\mathbf{J} \in \mathbb{R}^{N_V \times N_V}$ is the covariance matrix for the current density; and $[\mathbf{S}_\mathbf{J}]_{ii}$ is its i th diagonal element corresponding to the variance at the i th voxel. Note that localization inference is based on the images of unitless values z_i , and not on the current density $[\mathbf{J}]_i$.

There is no unique methodology for selecting the standard deviation $[\mathbf{S}_\mathbf{J}]_{ii}$ of the current density at each voxel. In the Bayesian formulation used by Dale *et al.* [27], it is assumed that the standard deviation for the current density at each voxel is due exclusively to measurement noise, i.e. only measurement noise contributes to the total EEG covariance. Their method is known as dynamic statistical parametric mapping (dSPM).

A very different derivation for the standard deviation is given by Pascual-Marqui [28], using a functional analysis formulation. This method is known as standardized low-resolution electromagnetic tomography (sLORETA). Unlike the

Dale *et al.* [27] method, it is assumed in sLORETA that the total EEG covariance receives contributions from noise in the scalp measurements and from neuronal generator noise.

A detailed comparison of the linear imaging methods of dSPM, sLORETA and the non-weighted minimum norm solution was performed using a realistic head model under ideal (low measurement noise) conditions in Pascual-Marqui [28]. All possible single-point test sources (Dirac deltas) were used for the generation of the scalp potentials, which were then given to each imaging method. Localization errors were defined as the distance between the location of the absolute maximum value ($|z_i|$ or $||\mathbf{J}_i||$) and the actual location of the test source. The mean location errors for the minimum norm method and for the Dale *et al.* [27] method were 38 and 34 mm, respectively. This indicates that the standardization of the Dale *et al.* method produces only a slight improvement over the minimum norm solution. The sLORETA method showed zero localization error under ideal (no-noise) conditions. These first empirical results demonstrated the zero-error property of sLORETA.

Soon after, theoretical proof for the zero-error property of sLORETA under ideal conditions was independently provided by Sekihara *et al.* [29] and Greenblatt *et al.* [30]. It was later shown theoretically that sLORETA has no localization bias, even in the presence of both measurement and biological noise [31].

(e) Exact low-resolution electromagnetic tomography

Historically, soon after the publication of the first tomography in this field in 1984, namely the non-weighted minimum norm solution [20], many attempts were made to improve the mislocalization of deep sources. A long sought solution has been to find an appropriate weight matrix \mathbf{W} in equation (2.10), such that the distributed linear inverse solution has zero localization error when tested with point sources anywhere in the brain, under ideal (no-noise) conditions.

The weights for exact localization with zero error under ideal (no-noise) conditions are obtained from the following nonlinear system of equations:

$$w_i = [\mathbf{K}_i^T (\mathbf{K}\mathbf{W}^{-1}\mathbf{K}^T + \alpha\mathbf{H})^+ \mathbf{K}_i]^{1/2}, \quad (2.13)$$

where w_i , for $i = 1, \dots, N_V$, are the elements of the diagonal weight matrix \mathbf{W} , and $\mathbf{K}_i \in \mathbb{R}^{N_E \times 1}$ denotes the i th column of the lead field matrix \mathbf{K} . Note that the weights depend nonlinearly on the lead field columns, but the inverse solution remains linear (equation (2.10)). Equation (2.13) corresponds to the algorithm for solving the weights (which do not depend on the measurements).

1. Initialize the diagonal weight matrix \mathbf{W} with elements $w_i = 1$, for $i = 1, \dots, N_V$.
2. Compute

$$\mathbf{C} = (\mathbf{K}\mathbf{W}^{-1}\mathbf{K}^T + \alpha\mathbf{H})^+. \quad (2.14)$$

3. Holding \mathbf{C} fixed, for $i = 1, \dots, N_V$, compute new weights

$$w_i = [\mathbf{K}_i^T \mathbf{C} \mathbf{K}_i]^{1/2}. \quad (2.15)$$

4. Using the new weights, go to step 2 until convergence (i.e. stop when the change in the weight matrix is sufficiently small).

Theoretical proof follows for the exact localization property of the linear inverse solution. From equation (2.10), the current density at the i th voxel is

$$[\mathbf{J}]_i = w_i^{-1} \mathbf{K}_i^T (\mathbf{K} \mathbf{W}^{-1} \mathbf{K}^T + \alpha \mathbf{H})^+ \Phi. \quad (2.16)$$

Substituting equation (2.13) into equation (2.16) gives

$$[\mathbf{J}]_i = [\mathbf{K}_i^T \mathbf{C} \mathbf{K}_i]^{-1/2} \mathbf{K}_i^T \mathbf{C} \Phi, \quad (2.17)$$

with \mathbf{C} given by equation (2.14). The squared current density $([\mathbf{J}]_i)^2$ can be shown to attain its maximum value when the actual scalp potential is generated by a point source at the target. For instance, a point source of strength a at the j th voxel gives

$$\Phi = a \mathbf{K}_j \quad (2.18)$$

and

$$([\mathbf{J}]_i)^2 = a^2 (\mathbf{K}_j^T \mathbf{C} \mathbf{K}_i)^2 (\mathbf{K}_i^T \mathbf{C} \mathbf{K}_i)^{-1}. \quad (2.19)$$

The partial derivative of the squared current density (equation (2.19)) with respect to \mathbf{K}_i gives

$$\frac{\partial}{\partial \mathbf{K}_i} ([\mathbf{J}]_i)^2 = 2a^2 (\mathbf{K}_j^T \mathbf{C} \mathbf{K}_i) (\mathbf{K}_i^T \mathbf{C} \mathbf{K}_i)^{-1} \mathbf{C} \{ \mathbf{K}_j - (\mathbf{K}_j^T \mathbf{C} \mathbf{K}_i) (\mathbf{K}_i^T \mathbf{C} \mathbf{K}_i)^{-1} \mathbf{K}_i \}, \quad (2.20)$$

which attains zero value when $\mathbf{K}_i = \mathbf{K}_j$.

This proves that the linear tomography in equation (2.10), with weights given by equation (2.13), solves the multi-variate inverse problem and, at the same time, achieves exact localization to test point sources under ideal (no-noise) conditions.

The linear tomography defined by equation (2.10) with weights given by equation (2.13) is denoted as exact low-resolution electromagnetic tomography (eLORETA) [6,31].

(f) *Exact low-resolution electromagnetic tomography validation*

eLORETA was tested under computer-controlled conditions, using a realistic head model, with 71 electrodes and 7002 cortical voxels. In this case, non-ideal conditions were used, with noise in measurements (signal to noise ratio SNR = 10), which will necessarily produce non-zero localization errors. Table 1 shows a number of performance measures for several weighted linear solutions; eLORETA outperforms all other linear solutions. In addition, simulations were carried out under ideal noiseless conditions, with eLORETA attaining zero localization error.

eLORETA was validated with real human EEG recordings obtained under diverse stimulation conditions, in order to verify the correct localization of activity in sensory cortices. Figure 1 shows correct localization of visual, auditory and somato-sensory cortices.

Table 1. Performance features for comparing regularized weighted minimum norm solutions, obtained under computer-controlled conditions, using a realistic head model with 71 electrodes and 7002 cortical voxels, with noise in measurements (signal to noise ratio SNR = 10). ‘MinNorm-0’ is the classical minimum norm solution [20]. ‘MinNorm-1’ is the weighted minimum norm solution as described in Lin *et al.* [26]. ‘eLORETA’ is the novel method presented here. ‘LocErr’ is the average localization error to 7002 point-test sources with randomly generated orientation. ‘MislocVol’ is a measure of mislocalized volume, defined as the average percent of voxels that have higher activation than the actual active voxel. ‘ROC-AUC-1’ is the area under the receiver operating characteristic (ROC) curve [32] for the collection of 7002 inverse solutions, each one owing to a point-test source. ‘ROC-AUC-2’ is the area under the ROC curve for a collection of 7002 inverse solutions, each one owing to a pair of point-test sources with randomly generated locations. Exact, non-ambiguous definitions of the performance measures can be found in the electronic supplementary material, methods.

	LocErr (mm)	MislocVol (%)	ROC-AUC-1	ROC-AUC-2
MinNorm-0	36.5881	8.7009	0.9341	0.8392
MinNorm-1	30.9908	3.6525	0.9697	0.8871
eLORETA	13.8669	0.5381	0.9947	0.9203

3. Intracranial coherence and phase synchronization

(a) Basic definitions

Dynamic functional connectivity between two brain regions will be quantified here as the ‘similarity’ between time-varying signals recorded at the two regions [33]. The generic term ‘similarity’ allows for a variety of measures that have been evaluated and used in the analysis of time series of electric neuronal activity. Quian-Quiroga *et al.* [34] and Dauwels *et al.* [35] provide excellent reviews.

Coherence provides a measure of linear similarity between signals in the frequency domain (e.g. [36]). Phase synchronization corresponds to a very particular form of nonlinear similarity. Both measures can be extended to time-varying Fourier transforms (or any complex valued wavelet transform).

Let x_{jt} and y_{jt} denote two stationary time series, with $j = 1, \dots, N_R$, denoting the j th segment or epoch. Define the real-valued vector

$$\mathbf{Z}_{jt} = \begin{pmatrix} x_{jt} \\ y_{jt} \end{pmatrix} \in \mathbb{R}^{2 \times 1}. \quad (3.1)$$

Its Fourier transform at frequency ω is denoted as

$$\mathbf{Z}_{j\omega} = \begin{pmatrix} x_{j\omega} \\ y_{j\omega} \end{pmatrix} \in \mathbb{C}^{2 \times 1}. \quad (3.2)$$

It will be assumed that x_ω and y_ω have zero mean. The Hermitian covariance, which is proportional to the cross-spectral matrix, is

$$\mathbf{S}_{ZZ\omega} = \frac{1}{N_R} \sum_{j=1}^{N_R} \mathbf{Z}_{j\omega} \mathbf{Z}_{j\omega}^* = \begin{pmatrix} s_{xx\omega} & s_{xy\omega} \\ s_{yx\omega} & s_{yy\omega} \end{pmatrix}, \quad (3.3)$$

where the superscript asterisk denotes transpose and complex conjugate.

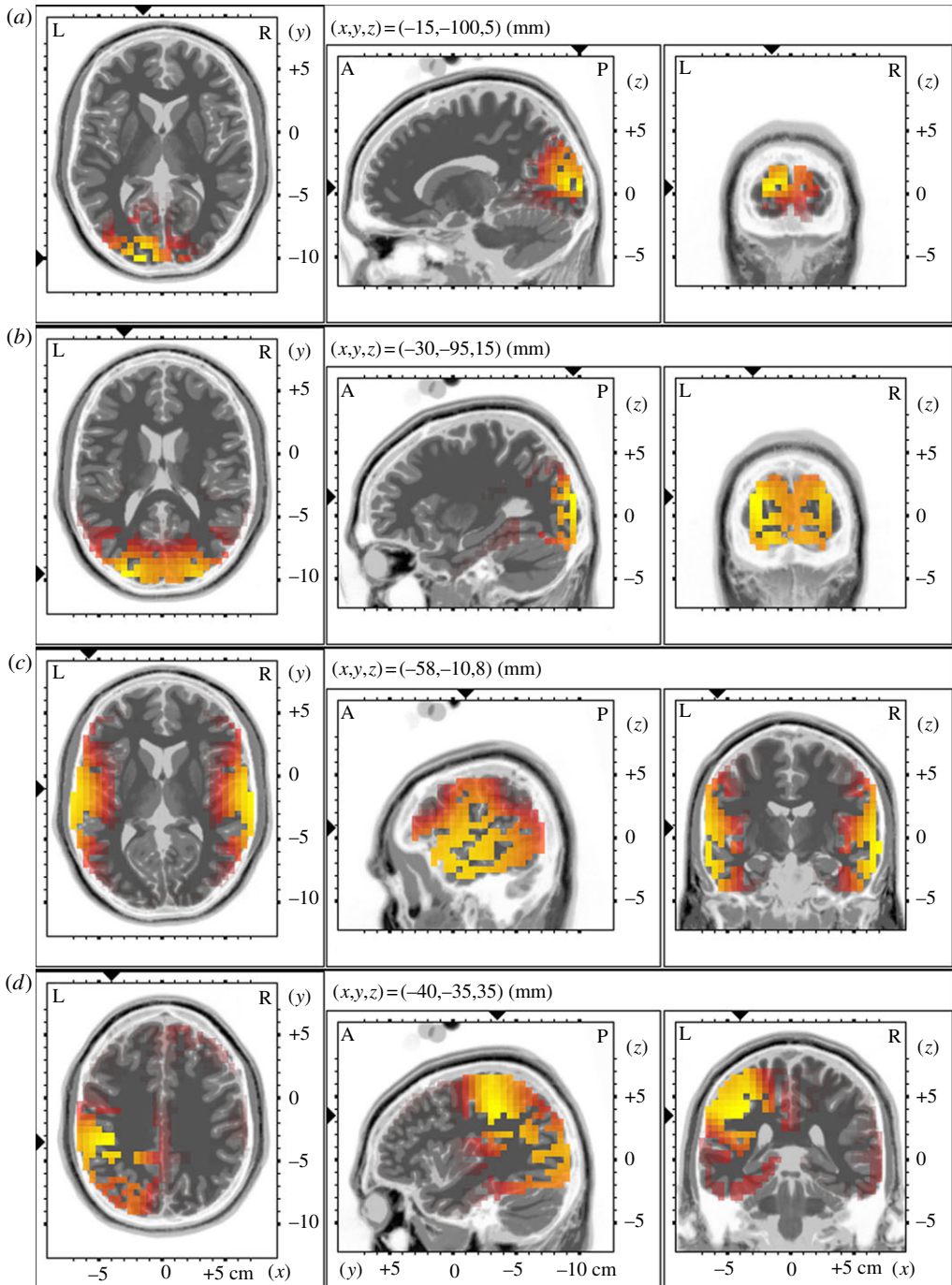


Figure 1. (Caption opposite.)

Figure 1. (*Opposite.*) Exact low-resolution brain electromagnetic tomography (eLORETA) applied to real human EEG recordings obtained under diverse stimulation conditions. The squared magnitude of the current density is colour coded from grey (zero) to red to bright yellow (maximum). Slices from left to right: axial (viewed from top), saggital (viewed from left), and coronal (viewed from back). L, left; R, right; A, anterior; P, posterior. Coordinates in Montreal Neurological Institute (MNI) space correspond to maximum activation, colour coded as bright yellow. (a) Right visual field stimulation with pattern-reversal checkerboard. Maximum activation in left Brodmann area (BA) 17. (b) Central visual field stimulation with white words on a black background. Maximum activation in BAs 17, 18, 19. (c) Auditory stimulation with tones. Maximum activation in bilateral temporal BA 42. (d) Somatosensory stimulation of the right hand. Maximum activation in left BA 2. (Online version in colour.)

A classic expression for the complex-valued coherence is

$$r_{xy\omega} = \frac{s_{xy\omega}}{\sqrt{s_{xx\omega}s_{yy\omega}}}. \quad (3.4)$$

Phase synchronization is equivalent to the coherence, but based on normalized (unit modulus) Fourier transforms, which gives it its nonlinear character. Formally, define the vector

$$\tilde{\mathbf{z}}_{j\omega} = \begin{pmatrix} \tilde{x}_{j\omega} \\ \tilde{y}_{j\omega} \end{pmatrix} \in \mathbb{C}^{2 \times 1}, \quad (3.5)$$

with $\tilde{x}_{j\omega} = x_{j\omega}/|x_{j\omega}|$ and $\tilde{y}_{j\omega} = y_{j\omega}/|y_{j\omega}|$ denoting the normalized Fourier transforms, which are complex numbers of the unit circle. This means that $s_{\tilde{x}\tilde{x}\omega} = s_{\tilde{y}\tilde{y}\omega} = 1$, and the complex valued phase synchronization is

$$\phi_{\omega} = \frac{s_{\tilde{x}\tilde{y}\omega}}{\sqrt{s_{\tilde{x}\tilde{x}\omega}s_{\tilde{y}\tilde{y}\omega}}} = s_{\tilde{x}\tilde{y}\omega}. \quad (3.6)$$

(b) Problems owing to volume conduction and low spatial resolution

The moduli of these measures (i.e. $|r_{\omega}|$ and $|\phi_{\omega}|$) are in the range zero (no similarity) to unity (perfect similarity). When these measures are computed for invasive intracranial recordings (i.e. for time series of local electric potential differences), they validly correspond to connectivity. However, for scalp EEG signals, it is invalid to assume that these measures establish connectivity between electrode sites, since electric neuronal activity does not project radially to the scalp. These connectivity measures can be validly applied to eLORETA signals, but must be corrected for bias towards higher values owing to the low spatial resolution of the method, which makes signals appear extremely similar at zero lag.

This problem has been dealt with previously in the literature, although the solutions were aimed at correcting for the volume conduction effect in scalp signals. Nolte *et al.* [37] proposed the use of the imaginary part of the coherence (denoted as r_{ω}^{im}) as an index of true physiological connectivity, and Stam *et al.* [38] proposed an estimator for the lagged part of phase synchronization.

(c) *The instantaneous and lagged frequency components of the total connectivity*

Here, we appropriately decompose the total connectivity into instantaneous and lagged contributions in such a way that the lagged component is minimally affected by the low spatial resolution artefact, thus containing almost pure physiological information. We follow the seminal work of Geweke [39], in which total connectivity is additively expressed in terms of instantaneous and Granger-causal components

$$F_{\text{Tot}} = F_{\text{Inst}} + F_{\text{Lag}}. \quad (3.7)$$

In particular, we use the observation by Parzen [40], which noted that these measures correspond to likelihood tests for different hypotheses on dependence.

Let

$$\mathbf{R}_{\mathbf{ZZ}\omega} = [\text{Diag}(\mathbf{S}_{\mathbf{ZZ}\omega})]^{-1/2} \mathbf{S}_{\mathbf{ZZ}\omega} [\text{Diag}(\mathbf{S}_{\mathbf{ZZ}\omega})]^{-1/2} \quad (3.8)$$

denote the coherence matrix, where $\text{Diag}(\cdot)$ is the diagonal matrix of the argument. The total connectivity measure (including instantaneous and lagged components) is proportional to the log-likelihood statistic for testing $H_0: \mathbf{R}_{\mathbf{ZZ}\omega} = \mathbf{I}$, which is

$$F_{\text{Tot}} = -\ln \text{Det}(\mathbf{R}_{\mathbf{ZZ}\omega}) = -\ln(1 - |r_{xy\omega}|^2), \quad (3.9)$$

where $\text{Det}(\cdot)$ denotes the determinant of the argument.

Next, we define the instantaneous (zero-lag) connectivity at discrete frequency ω . The direct, straightforward definition is based on the time domain zero-lag covariance of the filtered time series. For this purpose, consider the time series \mathbf{Z}_{jt} (equation (3.1)), and let $\mathbf{Z}_{jt}^{\omega\text{Filtered}}$ denote its filtered version to the single discrete frequency ω . The time domain zero-lag covariance is

$$\mathbf{A}_{\mathbf{ZZ}} = \frac{1}{N_{\text{T}}N_{\text{R}}} \sum_{t=1}^{N_{\text{T}}} \sum_{j=1}^{N_{\text{R}}} (\mathbf{Z}_{jt}^{\omega\text{Filtered}})(\mathbf{Z}_{jt}^{\omega\text{Filtered}})^{\text{T}}. \quad (3.10)$$

The instantaneous connectivity corresponds to the log-likelihood statistic for testing that the correlation matrix of $\mathbf{A}_{\mathbf{ZZ}}$ is the identity matrix. However, based on Parseval's theorem, the time-domain covariance $\mathbf{A}_{\mathbf{ZZ}}$ is proportional to the real part of the frequency-domain Hermitian covariance (equation (3.3)). Formally, the instantaneous (zero-lag) connectivity measure is proportional to the log-likelihood statistic for testing $H_0: \mathbf{R}_{\mathbf{ZZ}\omega}^{\text{re}} = \mathbf{I}$, which is

$$F_{\text{Inst}} = -\ln \text{Det}(\mathbf{R}_{\mathbf{ZZ}\omega}^{\text{re}}) = -\ln[1 - (r_{xy\omega}^{\text{re}})^2], \quad (3.11)$$

where the superscript 're' denotes the real part of the complex-valued matrix or number.

Finally, from equation (3.7), lagged (non-instantaneous) connectivity is

$$F_{\text{Lag}} = F_{\text{Tot}} - F_{\text{Inst}}, \quad (3.12)$$

which can be expressed explicitly as

$$F_{\text{Lag}} = \ln \frac{\text{Det}(\mathbf{R}_{\mathbf{ZZ}\omega}^{\text{re}})}{\text{Det}(\mathbf{R}_{\mathbf{ZZ}\omega})} = \ln \frac{1 - (r_{xy\omega}^{\text{re}})^2}{1 - |r_{xy\omega}|^2}. \quad (3.13)$$

Note that these measures of connectivity ‘ F ’ take values in the range zero (no similarity) to infinity (perfect similarity). They can be transformed to the $[0,1]$ interval, as a squared coherence or synchronization measure, by applying the transformation [41]

$$\rho^2 = 1 - \exp(-F). \quad (3.14)$$

Note however, that these squared coherences do not satisfy the additive property in equation (3.7).

Thus, the total squared coherence is the classical definition

$$\rho_{\text{Tot}}^2 = |r_{xy\omega}|^2 = (r_{xy\omega}^{\text{re}})^2 + (r_{xy\omega}^{\text{im}})^2, \quad (3.15)$$

where the superscript ‘im’ denotes the imaginary part. The instantaneous squared coherence is related to the real part of the coherence

$$\rho_{\text{Inst}}^2 = (r_{xy\omega}^{\text{re}})^2, \quad (3.16)$$

and the lagged squared coherence is

$$\rho_{\text{Lag}}^2 = \frac{(r_{xy\omega}^{\text{im}})^2}{1 - (r_{xy\omega}^{\text{re}})^2}. \quad (3.17)$$

These measures can be applied to the normalized Fourier transforms, as defined above (equations (3.5) and (3.6)), giving the same decomposition for the phase synchronization, where the lagged component is pure physiological, and affected minimally by low spatial resolution, which affects the instantaneous component.

This methodology has been generalized to include measures of similarity between two or more multi-variate time series [42]. Furthermore, the definitions extend directly to frequency bands, by using the pooled Hermitian covariance (equation (3.3) or based on phase information from equation (3.5)) over the group of discrete frequencies of choice.

We note that this approach can be applied to single discrete frequencies. For such a case, the autoregressive model degenerates and cannot be used, since the autoregression is deterministic and not stochastic for time series that are purely sinusoidal in nature. However, when the signals have a broad-band spectrum, the direct use of autoregressive type models can be very informative (e.g. [35,43,44]). A further limitation of the methods presented here is that the actual causality cannot be resolved when the signals are filtered to single frequencies, since the concept of lag for pure sinusoidal signals is ambiguous. This means the lagged connectivity measure cannot be unambiguously decomposed into two causal components, as is the case with autoregressive modelling of more complex signals (e.g. [45]).

(d) *A comparison of non-instantaneous connectivity measures*

We compare in a simple setting the new ‘lagged connectivity’ measure introduced here (ρ_{Lag}^2 in equation (3.17)), with the measure proposed by Nolte *et al.* [37] for true brain interaction, given by the imaginary part of the coherence

$$\rho_{\text{Nolte}}^2 = (r_{xy\omega}^{\text{im}})^2. \quad (3.18)$$

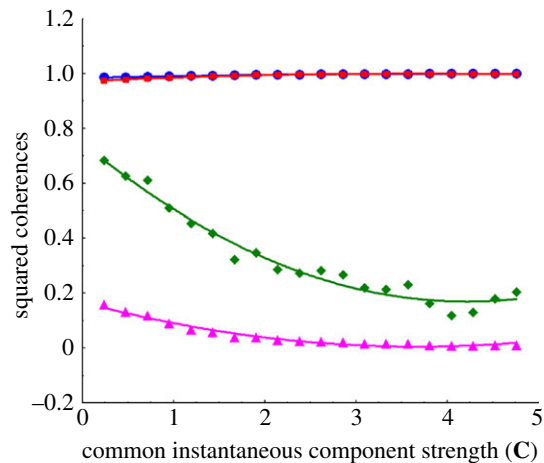


Figure 2. Total (filled circles), instantaneous (filled squares) and lagged (filled diamonds) measures of connectivity (this work); and the imaginary part (filled triangles) of the coherence [37]. Values were computed from simulated bivariate time series generated by a lagged component and an instantaneous component. The strength of the lagged component remained fixed (see description under equation (3.19)), while the strength of the common instantaneous (zero-lag) contribution (denoted as ‘ C ’ in the x -axis) was gradually increased. All coherences were computed at 8 Hz. Analyses at other frequencies showed the same general qualitative behaviour. (Online version in colour.)

Specifically, we generated data as

$$x_{jt} = \gamma c_{jt} + z_{j(t-1)} + d_{jt}$$

and

$$y_{jt} = \gamma c_{jt} + z_{jt} + e_{jt}, \quad (3.19)$$

where the time series c_{jt} , z_{jt} , d_{jt} and e_{jt} , were independent and identically distributed uniform random variables, with $c, z \sim U[-1, +1]$ and $d, e \sim U[-0.1, +0.1]$. The simulations consisted of using different values for γ in the range 0.2–4.8, and for each value, generating 500 epochs of 1 s duration each, sampled at 256 Hz. We computed the lagged connectivity (this work) and the imaginary part of the coherence [37], and show the results at 8 Hz frequency. Ideally, any change in the instantaneous component (determined by γ) should have little effect on the lagged or imaginary connectivities. Figure 2 shows that as the instantaneous component increases, both measures decrease, with the imaginary coherence tending to zero very quickly, while the lagged connectivity ρ_{Lag}^2 remains non-zero. The relative decrease is also much higher for the imaginary coherence.

The important point to note is that when there exists a lagged connection, the imaginary part of the coherence [37] fails to detect it by tending to zero if the instantaneous component is large. This is not the case for the lagged coherence in equation (3.17), which asymptotically tends to a non-zero value, detecting the presence of a physiological lagged connection.

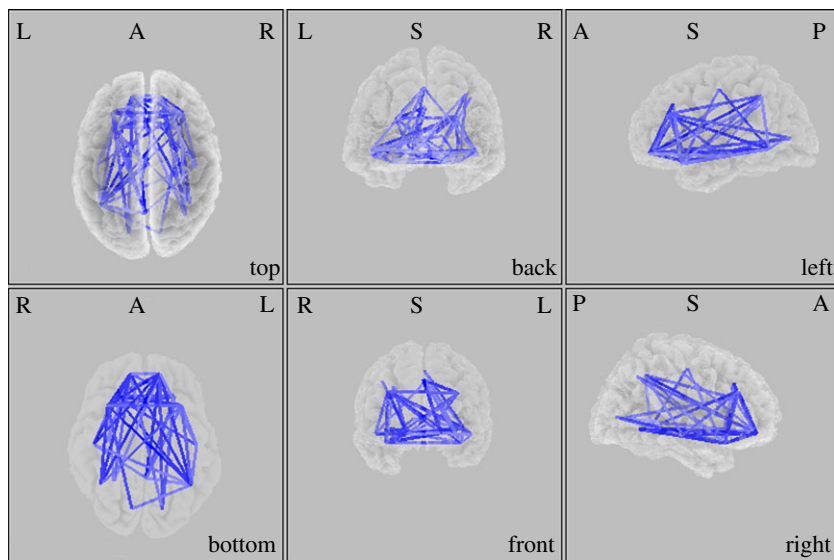


Figure 3. Wire diagram showing significantly disconnected regions in schizophrenia (blue wires). Widespread disconnection was observed, based on physiological lagged connectivity measures between cortical eLORETA signals. These results correspond to lower alpha (8.5–10 Hz) oscillations. (Online version in colour.)

(e) *An example: disconnections in schizophrenia*

In a previous study [46], the neuronal generators of oscillatory activity were compared between a group of patients with schizophrenia and a healthy control group. Specific patterns of cortical locations at specific EEG frequencies were observed to be different between the groups.

Using the same material [46], connectivity matrices were computed for the subjects in each group, for instantaneous and lagged connectivity measures (equations (3.11) and (3.13)). The intracranial signals were now computed with eLORETA, at 19 cortical sites, located under the electrodes of the 10/20 system. A statistical comparison of the connectivity matrices between the two groups was carried out, using non-parametric randomization techniques with correction for multiple testing.

No significant differences were found for the instantaneous connections. However, for the physiological lagged measure, a significant generalized, widespread disconnection was observed in schizophrenia, particularly notable in the theta and lower alpha bands. Figure 3 shows the significantly disconnected areas (as blue wires) in schizophrenia, for the lower alpha band (8.5–10 Hz). These results are in agreement with a number of other studies that report abnormal connectivity in schizophrenia (e.g. [47]).

4. Summary and outlook

We presented a new method for calculating cortical electric neuronal activity distributions from EEG measurements. This can be used for functional localization, as in classical neuroimaging; but more importantly, it provides

non-invasive intracranial recordings for the assessment of dynamic functional connectivity. We also presented a method for assessing connectivity between pairs of brain regions that is minimally affected by volume conduction and low spatial resolution, thus revealing pure physiological connectivity.

Using visual, auditory and somatosensory evoked responses obtained from different laboratories, eLORETA is shown to correctly localize function in the primary and secondary sensory cortices. This evidence validates the eLORETA method in terms of functional localization. Unfortunately, experimental data do not exist that can be considered as a gold standard for testing connectivity. Nevertheless, our connectivity analysis showing that schizophrenia is characterized by a highly disconnected brain is in general agreement with the literature.

These techniques provide information on brain function, in terms of localization and interactions. While there has been much development in statistics for the analysis of functional localization, there is still much need of tools for summarizing and interpreting connectivity data. Two approaches in the literature seem very promising: (i) graph-theoretical methods [48] and (ii) independent components and singular value decomposition methods [33,49]. Our next goal consists of adapting, extending and applying these connectivity analysis techniques to high time-resolution intracranial signals.

References

- 1 Lehmann, D. 1987 Principles of spatial analysis. In *Handbook of electroencephalography and clinical neurophysiology* (eds A. Gevins & A. Remond), pp. 309–354. Amsterdam: Elsevier.
- 2 Saletu, B., Anderer, P. & Saletu-Zyhlarz, G. M. 2006 EEG topography and tomography (LORETA) in the classification and evaluation of the pharmacodynamics of psychotropic drugs. *Clin. EEG Neurosci.* **37**, 66–80.
- 3 John, E. R., Pritchep, L. S., Fridman, J. & Easton, P. 1988 Neurometrics: computer-assisted differential diagnosis of brain dysfunctions. *Science* **239**, 162–169. (doi:10.1126/science.3336779)
- 4 Mitzdorf, U. 1985 Current source-density method and application in cat cerebral cortex: investigation of evoked potentials and EEG phenomena. *Physiol. Rev.* **65**, 37–100.
- 5 Martin, J. H. 1991 The collective electrical behavior of cortical neurons: the electroencephalogram and the mechanisms of epilepsy. In *Principles of neural science* (eds E. R. Kandel, J. H. Schwartz & T. M. Jessell), pp. 777–791. New York, NY: Elsevier.
- 6 Pascual-Marqui, R. D. 2009 Theory of the EEG inverse problem. In *Quantitative EEG analysis: methods and clinical applications* (eds S. Tong & N. Thakor), pp. 121–140. Boston: Artech House.
- 7 Sarvas, J. 1987 Basic mathematical and electromagnetic concepts of the biomagnetic inverse problem. *Phys. Med. Biol.* **32**, 11–22. (doi:10.1088/0031-9155/32/1/004)
- 8 Fuchs, M., Kastner, J., Wagner, M., Hawes, S. & Ebersole, J. S. 2002 A standardized boundary element method volume conductor model. *Clin. Neurophysiol.* **113**, 702–712. (doi:10.1016/S1388-2457(02)00030-5)
- 9 Pascual-Marqui, R. D. 1999 Review of methods for solving the EEG inverse problem. *Int. J. Bioelectromagnetism* **1**, 75–86.
- 10 Ary, J. P., Klein, S. A. & Fender, D. H. 1981 Location of sources of evoked scalp potentials: corrections for skull and scalp thicknesses. *IEEE Trans. Biomed. Eng.* **28**, 447–452. (doi:10.1109/TBME.1981.324817)
- 11 Mardia, K. V., Kent, J. T. & Bibby, J. M. 1979 *Multivariate analysis*. London, NY: Academic Press.
- 12 Lehmann, D. & Skrandies, W. 1980 Reference-free identification of components of checkerboard-evoked multichannel potential fields. *Electroencephalogr. Clin. Neurophysiol.* **48**, 609–621. (doi:10.1016/0013-4694(80)90419-8)

- 13 Hounsfield, G. N. 1995 Computerized transverse axial scanning (tomography): Part 1. Description of system. *Br. J. Radiol.* **68**, H166–H172. (Reprinted from *Br. J. Radiol.* **46**, 1016–1022, 1973)
- 14 Helmholtz, H. 1853 Ueber einige gesetze der vertheilung elektrischer strome in körperlichen leitern, mit anwendung auf die thierisch-elektrischen versuche. *Ann. Phys. Chem.* **89**, 211–233; 353–357. (doi:10.1002/andp.18531650603)
- 15 Tikhonov, A. & Arsenin, V. 1977 *Solutions to ill-posed problems*. Washington, DC: Winston.
- 16 Pascual-Marqui, R. D. 1995 Reply to comments by Hämäläinen, Ilmoniemi, and Nunez. In *Source localization: continuing discussion of the inverse problem* (ed. W. Skrandies), ISBET newsletter no. 6, pp. 16–28.
- 17 Tarantola, A. 2005 *Inverse problem theory and methods for model parameter estimation*. Philadelphia, PA: SIAM.
- 18 Valdes-Sosa, P. A., Vega-Hernandez, M., Sanchez-Bornot, J. M., Martinez-Montes, E. & Bobes, M. A. 2009 EEG source imaging with spatio-temporal tomographic nonnegative independent component analysis. *Hum. Brain Mapp.* **30**, 1898–1910. (doi:10.1002/hbm.20784)
- 19 Rao, C. R. & Mitra, S. K. 1973 Theory and application of constrained inverse of matrices. *SIAM J. Appl. Math.* **24**, 473–488.
- 20 Hamalainen, M. S. & Ilmoniemi, R. J. 1984 *Interpreting measured magnetic fields of the brain: estimates of current distributions*. Espoo, Finland: Helsinki University of Technology.
- 21 Axler, S., Bourdon, P. & Ramey, W. 1992 *Harmonic function theory*. New York, NY: Springer.
- 22 Hauk, O. 2004 Keep it simple: a case for using classical minimum norm estimation in the analysis of EEG and MEG data. *Neuroimage* **21**, 1612–1621. (doi:10.1016/j.neuroimage.2003.12.018)
- 23 Pascual-Marqui, R. D., Michel, C. M. & Lehmann, D. 1994 Low resolution electromagnetic tomography: a new method for localizing electrical activity in the brain. *Int. J. Psychophysiol.* **18**, 49–65. (doi:10.1016/0167-8760(84)90014-X)
- 24 Hamalainen, M., Hari, R., Ilmoniemi, R. J., Knuutila, J. & Lounasmaa, O. V. 1993 Magnetoencephalography: theory, instrumentation, and applications to noninvasive studies of the working human brain. *Rev. Mod. Phys.* **65**, 413–497. (doi:10.1103/RevModPhys.65.4133)
- 25 Grova, C., Daunizeau, J., Lina, J. M., Benar, C. G., Benali, H. & Gotman, J. 2006 Evaluation of EEG localization methods using realistic simulations of interictal spikes. *Neuroimage* **29**, 734–753. (doi:10.1016/j.neuroimage.2005.08.053)
- 26 Lin, F. H., Witzel, T., Ahlfors, S. P., Stufflebeam, S. M., Belliveau, J. W. & Hamalainen, M. S. 2006 Assessing and improving the spatial accuracy in MEG source localization by depth-weighted minimum-norm estimates. *Neuroimage* **31**, 160–171. (doi:10.1016/j.neuroimage.2005.11.054)
- 27 Dale, A. M., Liu, A. K., Fischl, B. R., Buckner, R. L., Belliveau, J. W., Lewine, J. D. & Halgren, E. 2000 Dynamic statistical parametric mapping: combining fMRI and MEG for high-resolution imaging of cortical activity. *Neuron* **26**, 55–67. (doi:10.1016/S0896-6273(00)81138-1)
- 28 Pascual-Marqui, R. D. 2002 Standardized low-resolution brain electromagnetic tomography (sLORETA): technical details. *Methods Find Exp. Clin. Pharmacol.* **24**(Suppl D), 5–12.
- 29 Sekihara, K., Sahani, M. & Nagarajan, S. S. 2005 Localization bias and spatial resolution of adaptive and non-adaptive spatial filters for MEG source reconstruction. *Neuroimage* **25**, 1056–1067. (doi:10.1016/j.neuroimage.2004.11.051)
- 30 Greenblatt, R. E., Ossadtchi, A. & Pflieger, M. E. 2005 Local linear estimators for the bioelectromagnetic inverse problem. *IEEE Trans. Signal Process.* **53**, 3403–3412. (doi:10.1109/TSP.2005.853201)
- 31 Pascual-Marqui, R. D. 2007 Discrete, 3D distributed, linear imaging methods of electric neuronal activity. Part 1: exact, zero error localization. (<http://arxiv.org/pdf/0710.3341>)
- 32 Kucukaltun-Yildirim, E., Pantazis, D. & Leahy, R. M. 2006 Task-based comparison of inverse methods in magnetoencephalography. *IEEE Trans. Bio-Med. Eng.* **53**, 1783–1793. (doi:10.1109/TBME.2006.873747)
- 33 Worsley, K. J., Chen, J.-I., Lerch, J. & Evans, A. C. 2005 Comparing functional connectivity via thresholding correlations and singular value decomposition. *Phil. Trans. R. Soc. B* **360**, 913–920. (doi:10.1098/rstb.2005.1637)

- 34 Quiroga, R. Q., Kraskov, A., Kreuz, T. & Grassberger, P. 2002 Performance of different synchronization measures in real data: a case study on electroencephalographic signals. *Phys. Rev. E* **65**, 041903. (doi:10.1103/PhysRevE.65.041903)
- 35 Dauwels, J., Vialatte, F., Musha, T. & Cichocki, A. 2010 A comparative study of synchrony measures for the early diagnosis of Alzheimer's disease based on EEG. *Neuroimage* **49**, 668–693. (doi:10.1016/j.neuroimage.2009.06.056)
- 36 Brillinger, D. R. 1981 *Time series: data analysis and theory*. New York, NY: McGraw-Hill.
- 37 Nolte, G., Bai, O., Wheaton, L., Mari, Z., Vorbach, S. & Hallett, M. 2004 Identifying true brain interaction from EEG data using the imaginary part of coherency. *Clin. Neurophysiol.* **115**, 2292–2307, (doi:10.1016/j.clinph.2004.04.029)
- 38 Stam, C. J., Nolte, G. & Daffertshofer, A. 2007 Phase lag index: assessment of functional connectivity from multi channel EEG and MEG with diminished bias from common sources. *Hum. Brain Mapp.* **28**, 1178–1193. (doi:10.1002/hbm.20346)
- 39 Geweke, J. 1982 Measurement of linear dependence and feedback between multiple time series. *J. Am. Stat. Assoc.* **77**, 304–313. (doi:10.2307/2287238)
- 40 Parzen, E. 1982 Comment on J. Geweke's 'Measurement of linear dependence and feedback between multiple time series'. *J. Am. Stat. Assoc.* **77**, 320–322. (doi:10.2307/2287242)
- 41 Pierce, D. A. 1982 Comment on J. Geweke's 'Measurement of linear dependence and feedback between multiple time series'. *J. Am. Stat. Assoc.* **77**, 315–316. (doi:10.2307/2287240)
- 42 Pascual-Marqui, R. D. 2007 Instantaneous and lagged measurements of linear and nonlinear dependence between groups of multivariate time series: frequency decomposition. (<http://arxiv.org/abs/0711.1455>)
- 43 Yamashita, O., Galka, A., Ozaki, T., Biscay, R. & Valdes-Sosa, P. 2004 Recursive penalized least squares solution for dynamical inverse problems of EEG generation. *Hum. Brain Mapp.* **21**, 221–235. (doi:10.1002/hbm.20000)
- 44 Galka, A., Yamashita, O., Ozaki, T., Biscay, R. & Valdes-Sosa, P. 2004 A solution to the dynamical inverse problem of EEG generation using spatiotemporal Kalman filtering. *Neuroimage* **23**, 435–453. (doi:10.1016/j.neuroimage.2004.02.022)
- 45 Kaminski, M., Ding, M. Z., Truccolo, W. A. & Bressler, S. L. 2001 Evaluating causal relations in neural systems: granger causality, directed transfer function and statistical assessment of significance. *Biol. Cybern.* **85**, 145–157. (doi:10.1007/s004220000235)
- 46 Pascual-Marqui, R. D., Lehmann, D., Koenig, T., Kochi, K., Merlo, M. C., Hell, D. & Koukkou, M. 1999 Low resolution brain electromagnetic tomography (LORETA) functional imaging in acute, neuroleptic-naive, first-episode, productive schizophrenia. *Psychiatry Res.* **90**, 169–179. (doi:10.1016/S0925-4927(99)00013-X)
- 47 Mulert, C., Kirsch, V., Pascual-Marqui, R., McCarley, R. W. & Spencer, K. M. 2011 Long-range synchrony of gamma oscillations and auditory hallucination symptoms in schizophrenia. *Int. J. Psychophysiol.* **79**, 55–63. (doi:10.1016/j.ijpsycho.2010.08.004)
- 48 Bullmore, E. & Sporns, O. 2009 Complex brain networks: graph theoretical analysis of structural and functional systems. *Nat. Rev. Neurosci.* **10**, 186–198. (doi:10.1038/nrn2575)
- 49 Calhoun, V. D., Liu, J. & Adali, T. 2009 A review of group ICA for fMRI data and ICA for joint inference of imaging, genetic, and ERP data. *Neuroimage* **45**, S163–S172. (doi:10.1016/j.neuroimage.2008.10.057)